BRIEF COMMUNICATION: SOL-GEL, HYBRIDS AND SOLUTION CHEMISTRIES

CrossMark

Engineering of large-pore lipid-coated mesoporous silica nanoparticles for dual cargo delivery to cancer cells

Achraf Noureddine[1] · Elizabeth A. Hjelvik[1] · Jonas G. Croissant[1] · Paul N. Durfee[1] · Jacob O. Agola[1] ·
C. Jeffrey Brinker[1,2]

Abstract

Lipid-coated mesoporous silica nanoparticles (LC-MSNs) have recently emerged as a next-generation cargo delivery nanosystem combining the unique attributes of both the organic and inorganic components. The high surface area biodegradable inorganic mesoporous silica core can accommodate multiple classes of bio-relevant cargos in large amounts, while the supported lipid bilayer coating retains the cargo and increases the stability of the nanocarrier in bio-relevant media which should promote greater bio-accumulation of LC-MSNs in cancer sites. In this contribution, we report on the optimization of various sol–gel synthesis (pH, stirring speed) and post-synthesis (hydrothermal treatment) procedures to enlarge the MSN pore size and tune the surface chemistry so as to enable loading and delivery of large biomolecules. The proof of concept of the dual cargo-loaded nanocarrier has been demonstrated in immortalized cervical cancer HeLa cells using MSNs of various fine-tuned pore sizes.

Graphical Abstract
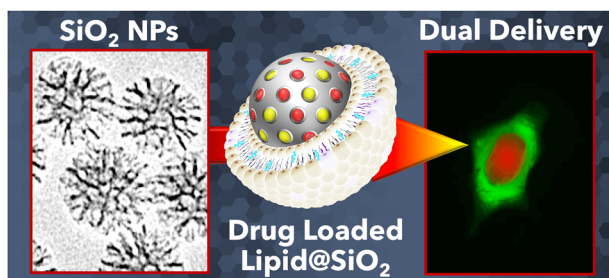
Highlights
- Lipid-coated mesoporous silica nanoparticles were prepared for dual cargo delivery to cancer cells.
- The pore and particle sizes, surface areas, and condensation degrees were tuned by sol–gel processes.
- Sol–gel (pH, stirring speed) and post-synthesis (hydrothermal treatment) parameters were optimized.

These authors contributed equally: Achraf Noureddine, Elizabeth A. Hjelvik.

✉ C. Jeffrey Brinker
cjbrink@sandia.gov

[1] Chemical and Biological Engineering, University of New Mexico, 210 University Blvd NE, Albuquerque, NM 87131-0001, USA

[2] Center for Micro-Engineered Materials, Advanced Materials Laboratory, University of New Mexico, MSC04 2790, 1001 University Blvd SE, Suite 103, Albuquerque, NM 87106, USA

1 Introduction

Mesoporous silica nanoparticles (MSNs) are one of the most studied and advanced drug delivery nanoplatforms for biomedical applications [1]. Using sol–gel science [2–5], monodispersed particles can be synthesized [2, 6] with tunable particle diameters ranging from 7 nm to several microns [1, 7–9]. In the context of cancer [10], controlling the size of the nanoparticles to below 200 nm allows for the enhanced permeation and retention effect to take place in order to accumulate nanoparticles (NPs) into tumors [11, 12]. MSNs have numerous additional assets such as tunable porosity (200–1200 $m^2 g^{-1}$), morphology (spherical [13, 14], core@shell [15, 16], rod-like and wire-like shapes [17, 18], etc.), and biodegradability from one day to several months [11]. MSNs are also biocompatible in high dosage and are excreted by animals and humans [11]. The engineering of the internal framework, as well as the external surface of MSNs, can be achieved via well-developed chemistry of silica using abundant surface silanol groups (~4.8 OH/nm^2) [1, 19–24]. Consequently, organically engineered mesoporous silica-based [25] nanomaterials have been applied for drug delivery via light [1, 26–29], magnetic [29–31], redox [32], enzymatic [33, 34], and pH [35–37] triggers, as well as for the delivery of biomolecules (e.g., siRNA, DNA) and multiple bio-active agents [1]. Multiple drug delivery, also called combination therapy, is a key strategy against drug-resistant cancers, as it enables synergistic effects via delivery of multiple therapeutic molecules dramatically enhancing cancer treatments [37, 38].

Lipid-coated mesoporous silica nanoparticles (LC-MSNs, also known as protocells) [39–41] are typically prepared by the fusion of a lipid vesicle [42] on an MSN core [6, 13, 43]. LC-MSNs have recently emerged as a next-generation of cargo delivery system combining advantages of both the organic and the inorganic worlds [43]. On the one hand, the biodegradable inorganic mesoporous [44] silica core provides a unique number of features when compared to other vectors such as liposomes alone including: (i) the possibility to straightforwardly load various bio-relevant cargos, (ii) controlled drug release, and (iii) bio-degradability [1]. On the other hand, the organic lipid component provides: (i) an increased stability of the nano-dispersion, (ii) a lower capture by the mononuclear phagocyte system, and (iii) a greater bio-accumulation of LC-MSNs into tumors [13, 43, 45]. LC-MSNs have been applied for active targeting and delivery of drugs to cancer cells [6, 45], multi-cargo delivery to cancer cells [13, 46], targeted antibiotic therapy [47], and DNA delivery [48] to name a few.

Controlling the pore structure and surface chemistry of MSNs is thus essential to design LC-MSNs for various biomedical applications such as multiple cargo delivery, where pore sizes exceeding those of the original MCM-41-type hexagonal mesoporous silica (~2.5 nm) are of interest. The increase of pore size of mesoporous silica materials was pioneered by Stucky and co-workers in 1998 with the so-called SBA-15 materials exhibiting 5–30 nm wide pores using the triblock copolymer P123 as a template [49]. However, the acid-catalyzed P123 strategy has proven to be largely incompatible with the preparation of sub-200 nm monosized MSNs needed for applications in nanomedicine. Hence, many approaches have been investigated to obtain large-pore MSNs [50–56], including the use of: (i) swelling agents added to the micelles [57], (ii) post-synthetic etching [58, 59], (iii) organosilane co-templating agents [60], and (iv) inorganic doping followed by calcination [29, 61].

In this study, we endeavored to assess the influence of various sol–gel synthesis parameters (pH, stirring speed) and post-synthesis manipulation (e.g., hydrothermal treatment (HT)) on directing the pore size of MSNs with the idea to create LC-MSNs capable of delivering multiple cargos (Fig. 1). The synthesis–property relationships were investigated via various techniques such as solid-state nuclear magnetic resonance (NMR) spectroscopy, nitrogen porosimetry, transmission electron microscopy (TEM), dynamic light scattering (DLS), and zeta potential (ζ) analyses. The panel of MSNs generated via tuning the above-mentioned parameters is found to variously impact: (i) the yield of the MSN synthesis, (ii) the condensation degree, (iii) the mesostructure, and most notably (iv) the pore size distributions of the particles.

2 Experimental section

2.1 Chemicals

Chemicals and reagents were used as received without further purification. All lipids, 1,2-distearoyl-sn-glycero-3-phosphocholine (DSPC), cholesterol, and (1,2-distearoyl-sn-glycero-3-phosphoethanolamine-N-[methoxy(poly-ethylene glycol)-2000] (ammonium salt) (DSPE-PEG) were purchased from Avanti Polar Lipids. Absolute (100%) and 95% ethanol (EtOH) were obtained from Decon Labs. Hydrochloric acid (HCl, 37%) and sodium hydroxide (NaOH, pellets) were purchased from Millipore Sigma

Fig. 1 Schematic representation of the sol–gel synthesis of mesoporous silica nanoparticles (MSNs) **a** and the parameters governing the optimization of the mesostructure **b**. Artistic representation of drug delivery to cancer cells via lipid-supported MSNs (LC-MSNs) **c**. CTAC cetyltrimethylammonium chloride (surfactant), TEOA triethanolamine (base)
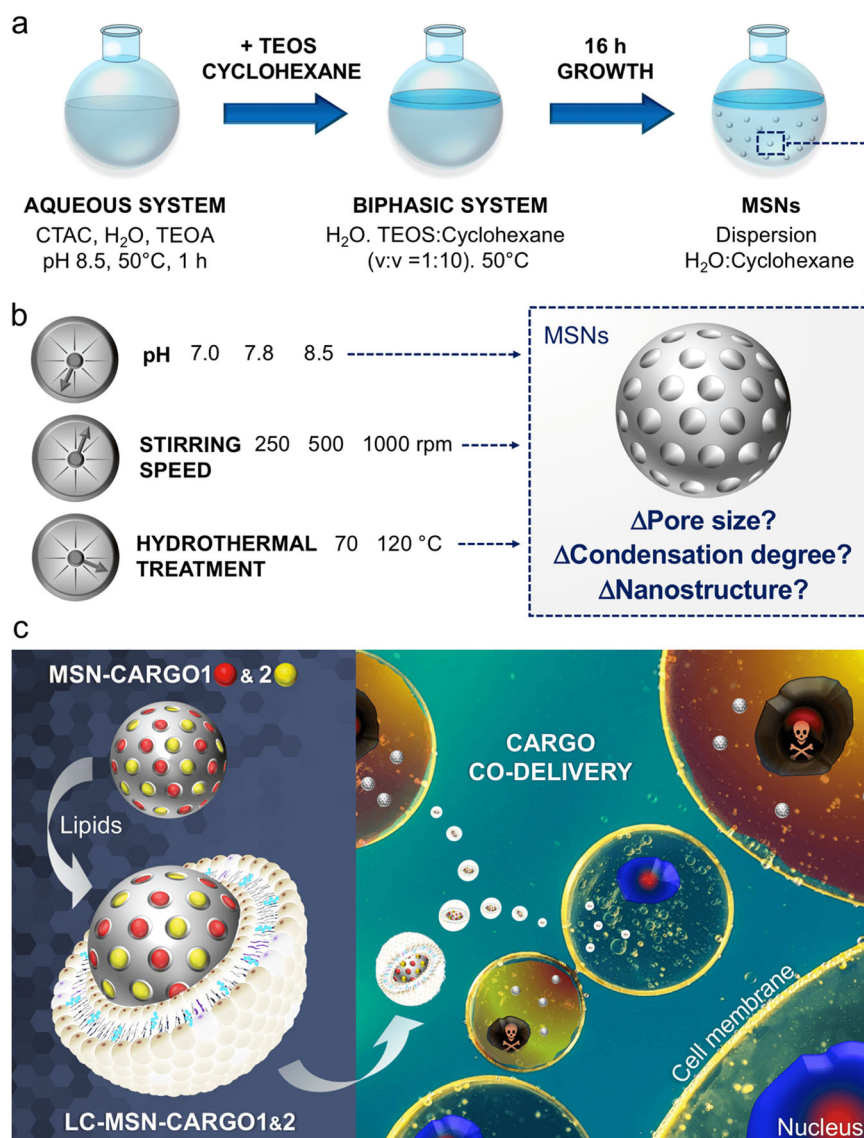
(formerly EMD Millipore). Ammonium nitrate (NH_4NO_3), cetyltrimethylammonium chloride (CTAC) 25% wt H_2O, cyclohexane, tetraethyl orthosilicate (TEOS), triethanolamine (TEOA) were purchased from Sigma-Aldrich (now Millipore Sigma). Doxorubicin hydrochloride was from TLC labs and Yo-Pro-1 iodide was from Thermo Fisher Scientific.

2.2 Characterization

TEM images were acquired on a JEOL 2010 (Tokyo, Japan) instrument equipped with a Gatan Orius digital camera system (Warrendale, PA) under a 200 kV voltage. Nitrogen adsorption–desorption isotherms of MSNs were obtained on a Micromeritics ASAP 2020 at 77 K. Samples were degassed at 60 °C for 12 h before measurements. The surface area was calculated following the Brunauer–Emmet–Teller (BET) equation and the pore size was obtained by DFT theory and standard Barrett–Joyner–Halenda (BJH) method from adsorption and desorption branches. Hydrodynamic size and zeta potential data were acquired on a Malvern Zetasizer Nano-ZS equipped with a He–Ne laser (633 nm) and non-invasive backscatter optics. All samples for DLS measurements were suspended in distilled water or ethanol at a 1 mg mL^{-1} concentration. Samples were washed three times through centrifugation prior to measurements. Measurements were acquired at 25 °C. DLS measurements for each sample were obtained in triplicate and then the Z-average diameter (by Intensity) was used for all reported hydrodynamic size values. The zeta potential for all the samples was measured in distilled water in triplicates according to Smoluchowski theory. All reported values correspond to the average of at three independent measurements.

2.3 General procedure for the synthesis of monodispersed dendritic large-pore MSNs without HT

In a 100 mL round bottom flask, 0.18 g (1.8 mmol) TEA, 24 mL (72.6 mmol) CTAC, and 36 mL of distilled water were stirred at 400 rpm and heated to 50 °C for an hour in order to bring the solution to temperature. The original pH of this solution was accordingly adjusted (pH 7.0, 7.8, or 8.5) using NaOH (2 M). Then, the stirring speed was adjusted in the order of 250, 500, or 1000 rpm before 20 mL of a solution of TEOS in cyclohexane (10% v/v) was added to form the biphasic system. The reaction was kept at 50 °C and under stirring rate (r) for 16 h. The mixture was then kept without stirring for 1 h and the top organic phase was removed (as much as possible). The bottom aqueous phase containing the NPs suspension was centrifuged and the isolated pellet washed in ethanol through successive sonication centrifugation steps. The removal of CTAC was achieved by washing the suspended particles in NH_4NO_3 (6 g L^{-1}) in ethanol followed by 1% HCl in ethanol. Each suspension was sonicated for 15 min and centrifuged accordingly. Each cycle of centrifugation was performed at 50 krcf for 15 min at room temperature. All MSNs samples were fully characterized and stored in pure ethanol. Syntheses of MSNs of the same category were conducted in parallel.

2.4 General procedure for synthesis of monodispersed dendritic large-pore MSNs with HT

The MSN synthesis was carried out following the same procedure described above. However, after removal of the organic phase, 16 h following TEOS addition and before the washing steps, the mixture was placed in the oven in a sealed hydrothermal reactor at 70 or 120 °C for 24 h. Following this step, the template extraction and sample storage were carried out the same way. The MSNs synthesis was carried out following the same procedure described above. However, after the organic phase removal 16 h following TEOS addition and before the washing steps, the mixture was placed in the oven in a sealed hydrothermal reactor at 70 or 120 °C for 24 h. Following this step, the template extraction and sample storage were carried as described above.

2.5 Liposomes preparation

Lipid solutions at 25 mg mL^{-1} in chloroform were stored at −25 °C under argon [6, 61]. 1,2-distearoyl-sn-glycero-3-phosphocholine (DSPC), cholesterol (chol), and (1,2-distearoyl-sn-glycero-3-phosphoethanolamine-N-[methoxy (polyethylene glycol) -2000] (ammonium salt) (DSPE-PEG) were mixed to the following molar ratio (75/20/5). The solvent was evaporated under reduced pressure for 16 h. The obtained film was hydrated by adding 1× PBS and ultra-sonicated in a sealed glass vial for 45 min at 40 °C in order to form a homogeneous suspension of liposomes at 5 mg mL^{-1}. The suspension was measured by DLS to confirm the good size and dispersity of liposomes.

2.6 Drug loading and lipids fusion

MSNs of choice (1 mg) in ethanol were centrifuged and washed with distilled water twice. The isolated pellet was then suspended in a doxorubicin hydrochloride solution (500 μL, 10 mg mL^{-1}) and kept overnight at room temperature for loading. Next, Yo-Pro-1 (63 μg, 100 μL, 1 mM in DMSO) was then added and the mixture was kept for another 16 h. Then, to the loading suspension of MSNs, the liposomal suspension was added under sonication (liposomes:MSNs 5:1 w/w) in order to fuse lipids on the surface of loaded MSNs. The obtained LC-MSNs were then centrifuged and washed with 1× PBS twice. All the supernatants were kept for drug loading quantitation. The dual drug loaded LC-MSNs were suspended in 1× PBS and used for internalization and cell viability assays in the following hour.

2.7 NP internalization and cell viability tests

HeLa cells were cultured at 37 °C and 0.5% CO_2 in T75 flasks using DMEM (Dulbecco's Modified Eagle's Medium) supplemented with 10% fetal bovine serum, L-glutamine, penicillin, and streptomycin. The cells were split every 2–3 days before plating. MSNs were synthesized according to the procedures described above and loaded with either doxorubicin alone or both doxorubicin and Yo-Pro-1 iodide. All loaded LC-MSN samples and control-free doxorubicin were suspended in 1× PBS solution at 1 mg mL^{-1} concentration before use. NP internalization and cell viability were assessed using a wide-field microscope (LEICA, Buffalo Grove, IL, USA) and CellTiter-Glo® Luminescent Cell Viability Assay kit (Promega, Madison, WI), respectively. The cell viability kit determines the number of viable cells based on the levels of ATP present, as a marker of metabolically active cells. This is scored by measuring the luminescence of the ATP-dependent oxygenation of luciferin by the luciferase enzyme which generates photo-unstable oxyluciferin intermediate. HeLa cells were seeded in two different ways. Cells for viability tests were seeded in a 96-well plate at a density of 7000 cells per well in 120 μL of DMEM medium, while cells for MSN internalization (through imaging) were seeded at a density of 1.5×10^5 cells mL^{-1} in a 6-well plate containing 25-mm

Table 1 Porosity parameter of MSNs obtained in various conditions

Variable parameter	No HT	HT 70 °C	HT 120 °C	250 rpm	500 rpm	1000 rpm	pH 7.0	pH 7.8	pH 8.5
Fixed parameters	250 rpm, pH 7.8			No HT, pH 7.8			No HT, 250 rpm		
BET SA ($m^2 g^{-1}$)	780	712	370	757	641	659	592	786	796
Pore volume ($cm^3 g^{-1}$)	2.01	2.74	1.4	1.98	1.78	1.76	1.14	1.87	2.19
Pore size									
BJH ads (nm)	10	16	39	8	10	12	7	10	13
BJH des (nm)	9	13–20	25	8	9	11	6–13	9–13	13
DFT (nm)	4; 10	4; 15–23	4; 29	3; 9	3; 11	3; 12	3; 15–20	3; 13–20	3; 13–20

HT hydrothermal treatment, *Rpm* rotation per minute

coverslip. After cell plating, both plates were incubated for 24 h at 37 °C and 0.5% CO_2 after which the cells for viability tests were incubated with either unloaded MSNs, doxorubicin-loaded MSNs, doxorubicin/Yo-Pro-1 iodide-loaded MSNs, or free doxorubicin. MSN concentrations were set at 25 or 100 µg mL^{-1} (final), while free doxorubicin was used at 0.1, 1, 10, and 20 µM. On the other hand, MSN internalization samples in the 6-well plate were incubated with a fixed concentration (25 µg mL^{-1}) of doxorubicin-loaded MSNs, doxorubicin/Yo-Pro-1 iodide-loaded MSNs, or free doxorubicin (10 µM final). Both plates were incubated for 12 h before cell viability tests and/ or imaging. Cell viability was scored by measuring luminescence after a 10-min incubation with the cell viability kit's buffer (Promega, Madison, WI), while imaging samples (on 25-mm coverslips) were fixed with 4% paraformaldehyde (15 min at room temperature) and rinsed twice with 1× PBS before imaging on the wide-field LEICA microscope. Control samples for viability tests included cells not exposed to either MSN or free doxorubicin. Percent cell viability was calculated relative to the luminescence of the control.

3 Results and discussion

3.1 LC-MSNs fabrication and characterization

The design of the MSNs was conducted according to a modified procedure of Zhao et al. [62]. In this procedure, as summarized in Fig. 1, an aqueous mixture of CTAC and TEOA was prepared at 50 °C and pH 7.0, 7.8, or 8.5, and then mixed with a solution of TEOS in cyclohexane to form a biphasic system (Fig. 1a). The stirring speed was varied (250, 500, or 1000 rpm) in order to assess the effect of the phase mixing rate on the nanostructure. Samples were then surfactant-extracted and a HT (70 or 120 °C) was carried out (or not) for the structure/pore optimization study (Fig. 1b). It is noteworthy that the yield of the syntheses
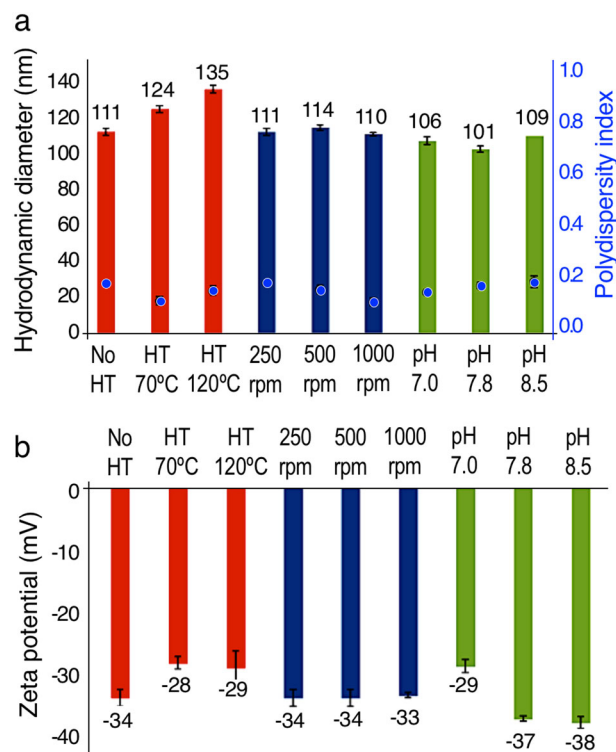

Fig. 2 Dynamic light scattering (DLS) **a** and zeta potential **b** analyses in water of MSNs obtained under various conditions

significantly varied with the studied conditions. The parameters used for establishing sol–gel synthesis–particle structure relationships are summarized in Table 1. In parallel, liposomal vesicles made of DSPC, cholesterol, and DSPE-PEG$_{2k}$ with a molar ratio of (75/20/5) were prepared by evaporation of chloroform from the stock solutions followed by rehydration in PBS to the concentration of 5 mg mL^{-1}. The liposomal vesicle suspension was characterized by DLS.

The key factors known to determine biodistribution/ in vivo behavior of MSNs such as the hydrodynamic diameter, size dispersity, and surface charge obtained under various synthetic conditions were first investigated by DLS
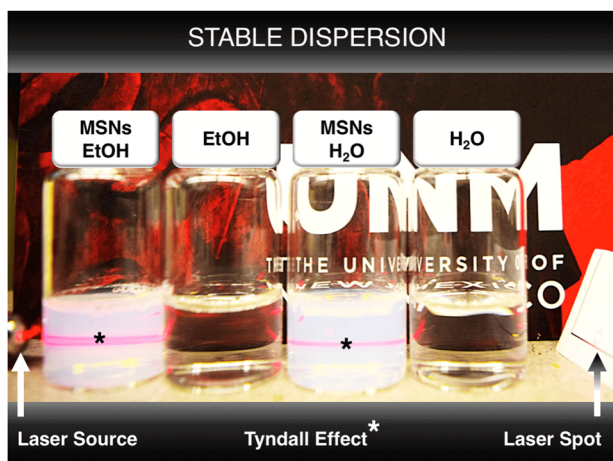
Fig. 3 Photograph showing the Tyndall effect on stable MSNs dispersions in ethanol and in water and the absence of any scattering in the corresponding pure dispersants (5 mg mL^{-1})

and zeta potential (ζ) analyses (Fig. 2). The measurements showed that all syntheses investigated in this study yielded monodispersed MSNs with a polydispersity index (PDI) below 0.2 and hydrodynamic diameters ranging from 100 to 130 nm (Fig. 2a). Very close hydrodynamic sizes results were obtained upon dispersing the MSNs in water or ethanol with very low statistical deviations (data not shown). Zeta potential analyses revealed the typical negatively charged surface of the MSNs (−28 to −38 mV) at neutral pH in aqueous media due to the presence of deprotonated surface silanol groups (SiO$^-$, SiO$_2$ isoelectric point ca. 2–3). The as-prepared surfactant-free MSNs were colloidal monosized particles (vide infra), and stable in different dispersants (see photographs in Fig. 3). The particles could be stably stored in ethanol for months without any aggregation.

3.2 Influence of HT on pore size

The influence of the post-synthesis HT on the porosity and the morphology of MSNs was then investigated. MSNs were synthesized at a fixed pH (7.8) and then stirred at 250 rpm before carrying out (or not) HT at 70 or 120 °C. TEM analyses displayed monosized non-aggregated MSNs with pore sizes increasing as a function of the HT temperature (Fig. 4a–c). Note that the larger hydrodynamic diameters calculated by DLS, when compared with TEM images, are the result of the water layer surrounding the particles (10–20 nm, hence an overestimation of about 20–40 nm) which impacts the light scattering measurements. Before HT, the dendritic growth of the silica network around concentrated surfactant/swelling agents formed radial pores, as observed by TEM images (Fig. 4a). An increase in the HT temperature appeared to lower the silica density of the MSNs

(lower particle contrast from Fig. 4a–c) as shown by thinner pore frameworks with larger pores at 70 °C (Fig. 4b) and eventual etching of the framework (with some eventual rearrangement) to form interesting star-like MSNs at 120 °C (Fig. 4c). These observations were confirmed by N$_2$ sorption data with surface areas decreasing in the order of 780, 712, and 370 m^2 g^{-1} against respective increase in pore sizes of 9, 15, and 25–30 nm, for the following conditions: without HT, 70 °C HT, and 120 °C HT (Fig. 5a, d). The surface areas and pore size distributions were, respectively, calculated using the BET and BJH sorption theories. HT thus caused the progressive etching/condensation of the silica pore walls to form larger pores. Finally, the HT was demonstrated to affect the yield of the reaction that decreased from 20 to 8% when the mixture was subjected to 70 and 120 °C HT, respectively (Fig. 6). Actually, the silica cross-linking is highly affected by temperature (Tables 2 and 3); the sol–gel hydrolysis and condensation reactions inducing the loss of ethanol and water molecules were accentuated at higher temperatures. Also, the etching process we highlighted played a key role in lowering the final weight of yielded MSNs.

3.3 Influence of synthesis stirring speed on pore size

After outlining the effect of HT, the influence of the synthesis stirring speed (i.e., organic/aqueous phases mixing rate) on the porosity and morphology of MSNs was then investigated. MSNs were synthesized at a fixed pH (7.8) using various mixture stirring speeds (250, 500, or 1000 rpm) without post-synthesis HT. The stirring speed dictates the aqueous/organic interface area and thus the interaction between the silica precursor and the surfactant/catalyst system. Therefore, tuning the stirring speed is another controllable parameter we chose to fine-tune the pore size, in a shorter range, and without subjecting MSNs to any HT. TEM images showed spherical monosized non-aggregated MSNs for all the stirring speeds and a more defined structure with increased porosity at the highest stirring speed (Fig. 4d–f). The higher the stirring speed, the more important the interface between the organic phase (containing silica precursor and swelling agent) and the aqueous phase (catalyst and surfactant) becomes, a phenomenon which not only induces a higher hydrolysis/condensation rate but also higher rates of cyclohexane-induced micelle swelling. The increase of the stirring speed was associated with increased pore sizes from 8 to 11–15 nm (average BJH data) with BET surface areas of about 750 to 650 m^2 g^{-1} (Fig. 5b, e). The enhanced reaction kinetics caused by the higher stirring speeds likely increased the diameter of CTAC micelles upon increasing swelling agent incorporations during the sol–gel process. Herein, the yield of the reactions was a function of the stirring speed, which determines the
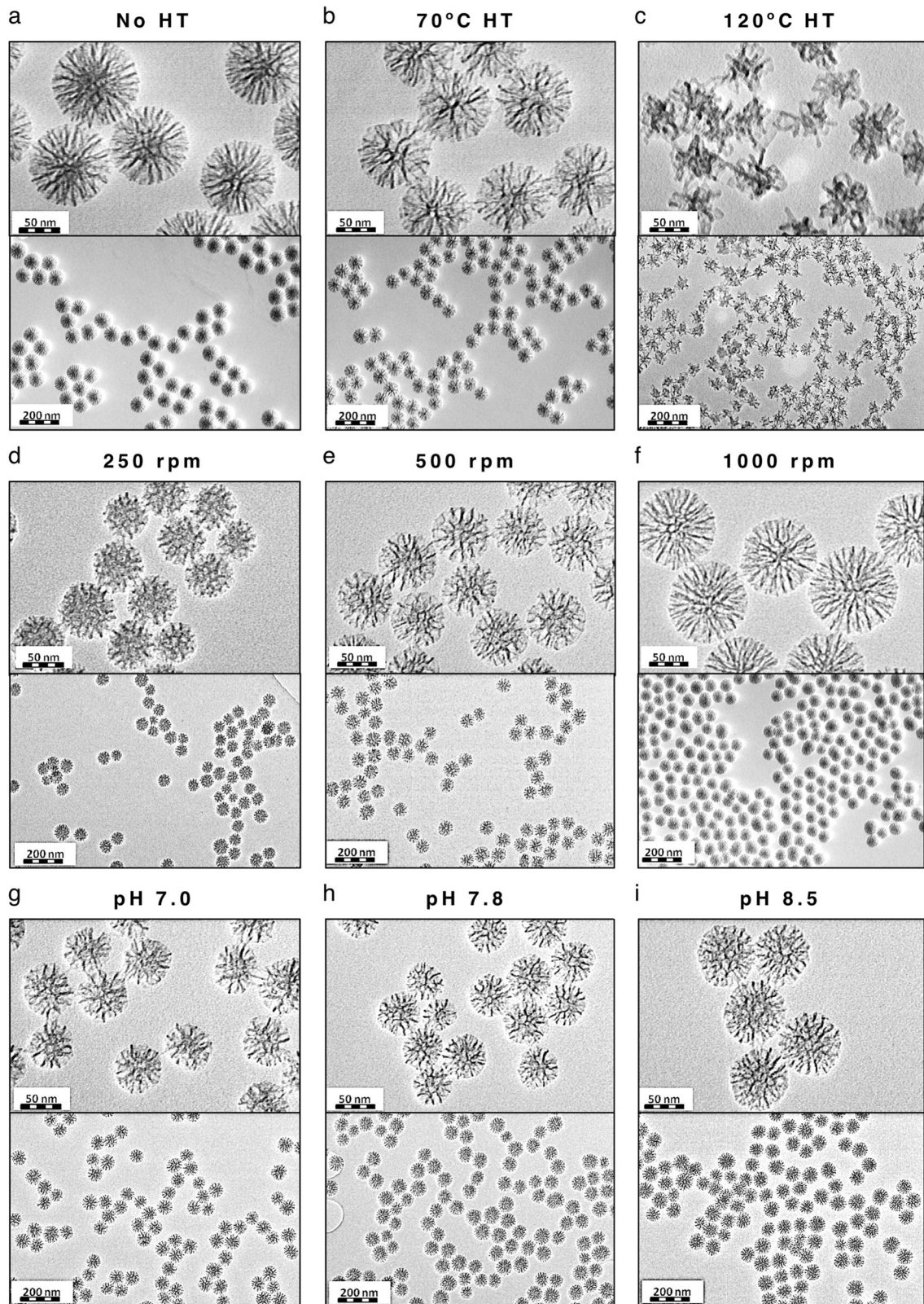
Fig. 4 TEM images displaying the influence of hydrothermal treatments (or absence thereof) on the pore size and morphology of MSNs **a–c**, the influence of the stirring speed during the synthesis on the pore size of MSNs **d–f**, and the influence of the pH on the pore size of MSNs during the synthesis process **g–i**
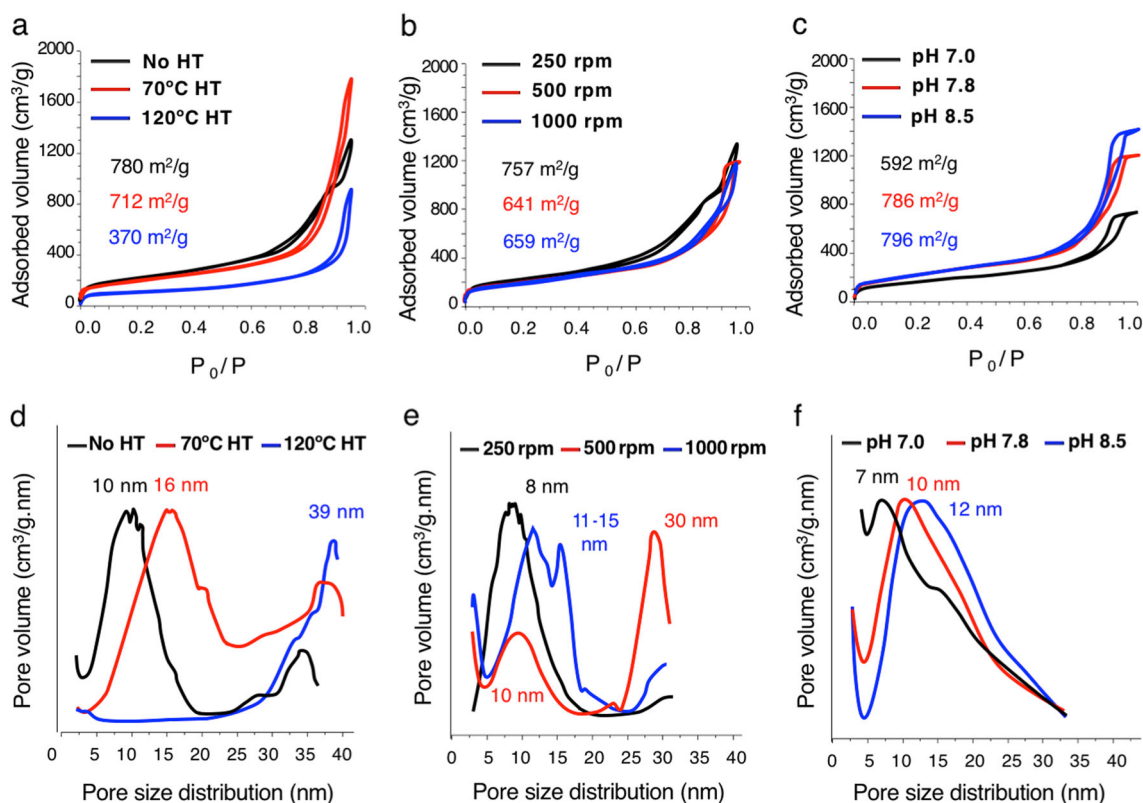
Fig. 5 Nitrogen sorption isotherms **a–c** and pore size distributions (BJH from the adsorption branches) **d–f** of MSNs obtained after (or without) hydrothermal treatment **a**, **d**, and under various stirring speed **b**, **e** and pHs **c**, **f**
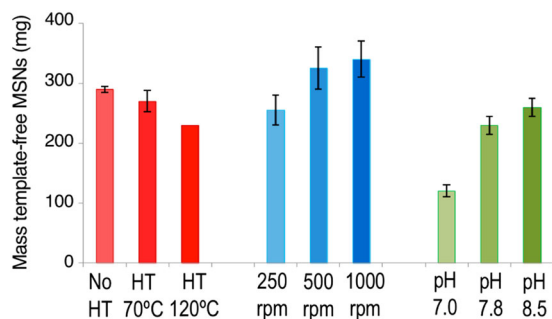

Fig. 6 Resulting masses of the MSN samples obtained under various synthetic conditions. The results are an average of three batches (with the exception of HT 120 °C) and were used for the yield calculations

interfacial area between TEOS-containing organic phase and the aqueous phase containing the catalyst and the surfactant. Increasing the stirring speed will spontaneously induce more silica precursors to undergo interfacial sol–gel reactions and thereby increasing the yield of MSNs.

3.4 Influence of the pH of the reaction on pore size

The influence of the pH on the porosity and the morphology of MSNs was then investigated. MSNs were synthesized at a fixed stirring speed (250 rpm) and at various pH (7, 7.8, or

8.5) conditions without post-synthesis HT. The impact of the pH on the diameter of silica particle was minimal as shown by monodispersed particle size distributions centered at ca. 70 nm for all the pH conditions tested (Fig. 4h–i). Incremental enhancements of BJH pore distributions were observed from nitrogen sorption measurements as the pH of the solution was increased (Fig. 5c, f). This could be the result of larger micelles packing at higher pH values. In all cases, pore size distributions obtained by density functional theory (DFT) showed the presence of a pore family at 3–4 nm, most likely originating from the domains of CTAC micelles with a lower cyclohexane swelling effects (Table 1). The basic pH promotes the silica condensation mechanism and exhibited the highest yield (~100% more than neutral pH).

3.5 Influence of HT, stirring speed, and reaction pH on the silica cross-linking

The effect of fine-tuning the aforementioned parameters on the condensation degree of silica particles was then assessed via ^{29}Si solid-state NMR. Proton polarization decoupling (HPDEC) NMR sequences were applied to quantify the type of silicon environments present (Fig. 7, Table 2). The various ^{29}Si populations appeared at different chemical

**Table 2** Condensation degrees of MSNs based on HPDEC ^{29}Si NMR

^{29}Si signal	No HT	HT 70 °C	HT 120 °C	250 rpm	500 rpm	1000 rpm	pH 7.0	pH 7.8	pH 8.5
Q^4 (%)	30	33	38	30	33	40	25	29	38
Q^3 (%)	52	59	53	52	57	50	55	59	48
Q^2 (%)	18	8	9	18	10	10	19	12	14
Cross-linking degree (%)	43	48	61	43	49	67	34	41	62

The cross-linking degree (%) was calculated as $Q^4/(Q^2 + Q^3)$. *HT* hydrothermal treatment, *rpm* rotation per minute (various HT were done at 250 rpm, pH 7.8; various rpm were done with no HT, pH 7.8; various pH were done with no HT, 250 rpm)

Table 3 Condensation degrees of MSNs based on ^{29}Si CP-MAS NMR

^{29}Si signal	No HT	HT 70 °C	HT 120 °C	250 rpm	500 rpm	1000 rpm	pH 7.0	pH 7.8	pH 8.5
Q^4 (%)	13	13	14	12	13	14	15	NA	11
Q^3 (%)	78	78	78	82	77	81	78	NA	80
Q^2 (%)	9	9	7	6	10	5	7	NA	9
Cross-linking degree (%)	15	15	17	14	14	17	18	NA	13

The cross-linking degree (%) was calculated as the ratio of chemical shifts of Q^4 to $(Q^2 + Q^3)$. *HT* hydrothermal treatment, *rpm* rotation per minute (various HT were done at 250 rpm, pH 7.8; various rpm were done with no HT, pH 7.8; various pH were done with no HT, 250 rpm)
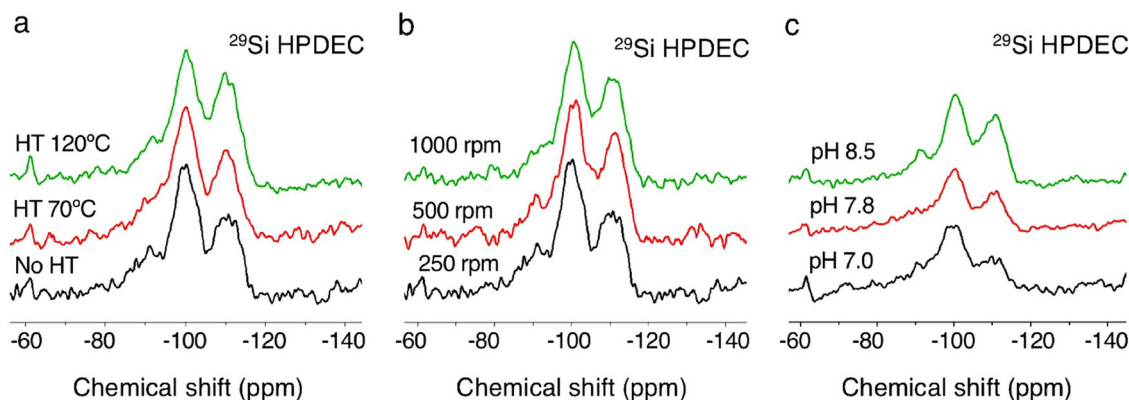
Fig. 7 HPDEC ^{29}Si NMR spectra of MSNs obtained under various conditions

shifts near −90, −100, and −110 ppm, respectively corresponding to Q^2 [(HO)$_2$Si(OSi)$_2$], Q^3 [(HO)Si(OSi)$_3$], and Q^4 [Si(OSi)$_4$] silicon local environments. The integration of these populations was performed to estimate the silica cross-linking degree, also called the condensation degree, according to the following equation: $Q^4/(Q^2 + Q^3)$ (see Tables 2 and 3). The sol–gel process being both thermodynamically and kinetically governed, the silica cross-linking degree was unsurprisingly found to increase with parameters affecting the reaction kinetics. First, the higher the HT temperature was, the higher the silica cross-linking degree became, starting with 43% without HT, to 48% with 70 °C HT, and 61% with 120 °C HT (Table 2). Higher temperatures are indeed known to promote the formation of siloxane groups from surface silanols through dehydration

reactions, as shown by the lower zeta potentials obtained in these materials (Fig. 2b). Second, the higher the stirring speed was, the higher the cross-linking degree became, ranging from 43 to 67% (Table 2). Evidently, higher stirring speeds accelerated sol–gel processes and thus indirectly the eventual condensation degree.

The same trend was also found by changing the initial pH of the solution. As the silica condensation process is favored in a basic environment, the cross-linking degree of MSNs was as expected found to be the highest (62%) at pH 8.5 and decreased to 41 and 34% when lower initial pH values (7.8 and 7.0, respectively) were used.

Additionally, non-quantitative ^{29}Si cross-polarization magic-angle-spinning (CPMAS) analyses were also performed and showed the predominance of Q^3 peaks (~80%)
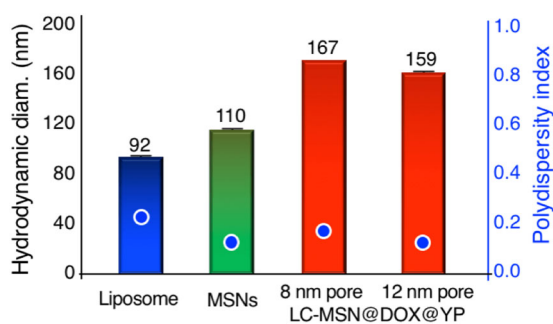
Fig. 8 Dynamic light scattering analyses in water of a Liposome control, MSNs, and dual-loaded LC-MSNs of 8 or 12 nm wide pore sizes. The trend of the diameter increase is consistent with the formation of the nanovectors

for all the samples. This validated the low condensation degrees in the various MSNs as a result of high silanol contents, enabling the cross-polarization to proximal silicon atoms (S1). Importantly, low condensation degrees in silica nanomaterials has been demonstrated to generate the rapid degradability of the NPs in biological media via dissolution into biocompatible silicic acid byproducts, which in turn favors a complete renal clearance in a few weeks after injection in animal and humans [11, 62].

At this point MSNs with different pore sizes were loaded with dual cargos and coated with lipid bilayers as a proof of concept of combination therapy packaging and delivery. As mentioned earlier, the delivery of multiple drugs exhibiting synergistic effects is promising for the treatment of drug-resistant cancers and has demonstrated dramatic enhancement of therapeutic efficacies [37, 38]. Particles with average pore size distribution of 8 and 12 nm were thus selected and loaded with two different cargos, namely, the doxorubicin hydrochloride (DOX) anti-cancer drug and the YO-PRO-1 Iodide (YP) nucleic acid fluorescent probe. Note that YP biomarker permeates into apoptotic cells and causes a green nuclear staining but is impermeant to healthy cells. Next, the dual-loaded MSNs were coated with a lipid bilayer through the addition of freshly prepared liposomes to a cargo-loaded MSN suspension. The loading capacities of DOX and YP were calculated by UV-Vis analyses of cargo loading supernatants and were respectively of 22 and 4 wt% for the 8 nm-LC-MSNs and increased to 33 and 6 wt% for 12 nm-LC-MSNs. The increase of hydrodynamic size proves the insertion of additional layers onto MSNs surface and the low PDI is also indicative of the system stability in PBS thanks to the supported lipid bilayer (Fig. 8). It is noteworthy that LC-MSN loaded solely with DOX presented larger initial size (~220 nm) and tended to aggregate over time (Fig. 8). This instability can be rationalized by the fact that, for larger pores MSNs, a dual loading may be crucial to fill in the pores inducing sufficient attractive van der Waals interactions and reducing surface roughness so as
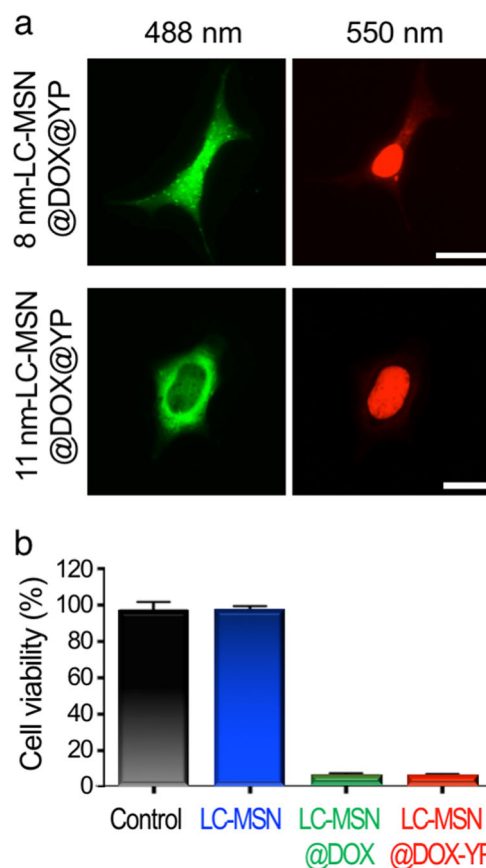

Fig. 9 Representative confocal microscopy images of HeLa cells with the green ($\lambda_{ex} = 488$ nm; $\lambda_{em} = 509$ nm) and red ($\lambda_{ex} = 550$ nm; $\lambda_{em} = 570$ nm) channels demonstrating the co-delivery of Yo-Pro1 and DOX cargos with LC-MSNs with 8 and 12 nm wide pores (upper and lower rows, respectively) **a**. Scale bars: 25 μm. HeLa cell viability studies demonstrating the cell killing associated with the delivery of DOX anti-cancer drug via nanomaterial incubations at 25 μg mL^{-1} **b**

to promote vesicle fusion on the drug-loaded MSN core. The proof of concept of the cargo co-delivery was then demonstrated in cervical cancer HeLa cells. The cells were incubated with nanomaterials at a concentration of 25 μg mL^{-1}. The dual delivery of the cargos via 8 nm-LC-MSNs and 12 nm-LC-MSNs was clearly observed via wide-field microscopy images displaying the green and red cellular staining typical of YP and DOX molecules, respectively (Fig. 9a). The red nuclear staining of DOX drug was similar for the porous LC-MSNs of the two different pore sizes and typical of the anti-cancer activity of DOX based on its DNA intercalation. Interestingly, the green staining of YP differed significantly with the size of the pores of LC-MSNs. The 8 nm-LC-MSNs led to a diffused green color throughout the cytoplasm suggesting that the YP was partially released into the cytoplasm while a fraction remained loaded into the nanocarriers (Fig. 9, upper row). The 12 nm-LC-MSNs, however, produced a perinuclear accumulation of the green color suggesting possible transient trafficking of YP

molecules to the nucleus (Fig. 9, lower row). The larger pore size of 12 nm-LC-MSNs may account for the faster diffusion rate and delivery of YP cargos though further biological investigations would be valuable to assess the internalization pathway and release kinetics obtained with various nanoplatforms. Finally, the biocompatibility of LC-MSNs was confirmed in HeLa cells along with the cancer treatment capability via delivering DOX drugs via 8 nm-LC-MSNs (Fig. 9b). The same results were obtained for 11 nm-LC-MSNs with a nearly total cell killing with single and dual cargo-loaded nanovectors.

4 Conclusion

In summary, we investigated the influence of various synthetic factors such as the pH, the stirring speed, and the post-synthesis HT on the size, porosity, and condensation degree of dendritic mesoporous silica nanomaterials. The panel of materials obtained via tuning the above-mentioned parameters yielded the following trends:

- Higher synthetic stirring speeds (250–1000 rpm) correlated with incremental pore size increases (8–12 nm) and higher silica condensation degrees (43–67%) without affecting the particle size (ca. 70 nm).
- Higher synthetic pHs (7.0–8.5) correlated with significant pore size increases (7–15 nm) and lower silica condensation degrees (62–42%) without affecting the particle size (ca. 70 nm).
- The implementation of HTs (70 or 120 °C) caused important pore size increases (10–39 nm) and higher silica condensation degrees (43–61%) with drastic changes in the mesostructured and morphology of the particles. Original star-like NPs were obtained after HTs at 120 °C.

All these synthetic procedures could be used to prepare biodegradable highly monodispersed spherical particles of hydrodynamic diameter near 120 nm with high porosities ($S_{BET} = 370$ to $800 \, m^2 \, g^{-1}$) useful for biomedical applications. The synthesized large-pore MSNs have been successfully dual-loaded with a chemotherapeutic (doxorubicin) and an apoptotic cell probe (Yo-Pro-1) and exhibited very high loading capacity. Importantly, we showed that dual loading of the aforementioned cargo molecules had a crucial role in the successful coating of large-pore MSNs with lipid bilayers. Finally, the proof of concept of dual cargo delivery was demonstrated in vitro in cancer cells. Differences in the apparent kinetics of cargo delivery call for further studies of the influence of the NP pore size on their internalization pathways and delivery capabilities. Tuning the delivery rate of various drugs is, in fact, a key advantage of NP-based drug co-delivery over the use of drug mixtures and could open combination therapy approaches most effective for multi-drug-resistant cancers.

Compliance with ethical standards

Conflict of interest The authors declare that they have no conflict of interest.

References

1. Croissant JG, Fatieiev Y, Almalik A, Khashab NM (2018) Mesoporous silica and organosilica nanoparticles: physical chemistry, biosafety, delivery strategies, and biomedical applications. Adv Healthc Mater 7:1700831
2. Brinker CJ, Scherer GW (1990) Sol-gel science: the physics and chemistry of sol-gel processing. Academic Press, Boston
3. Jiang X, Bao L, Cheng Y-S, Dunphy DR, Li X, Brinker CJ (2012) Aerosol-assisted synthesis of monodisperse single-crystalline α-cristobalite nanospheres. Chem Commun 48:1293–1295
4. Jiang X, Jiang Y-B, Brinker CJ (2011) Hydrothermal synthesis of monodisperse single-crystalline alpha-quartz nanospheres. Chem Commun 47:7524–7526
5. Lu Y, Ganguli R, Drewien CA, Anderson MT, Brinker CJ, Gong W, Guo Y, Soyez H, Dunn B, Huang MH, Zink JI (1997) Continuous formation of supported cubic and hexagonal mesoporous films by sol–gel dip-coating. Nature 389:364–368
6. Durfee PN, Lin YS, Dunphy DR, Muñiz AJ, Butler KS, Humphrey KR, Lokke AJ, Agola JO, Chou SS, Chen IM, Wharton W, Townson JL, Willman CL, Brinker CJ (2016) Mesoporous silica nanoparticle-supported lipid bilayers (protocells) for active targeting and delivery to individual leukemia cells. ACS Nano 10:8325–8345
7. Shenoi-Perdoor S, Noureddine A, Dubois F, Wong Chi Man M, Cattoën X (2016) Click functionalization of sol–gel materials. Handbook of sol-gel science and technology. Springer, Cham, pp 1–40
8. Noureddine A, Lichon L, Maynadier M, Garcia M, Gary-Bobo M, Zink JI, Cattoen X, Wong Chi Man M (2015) Controlled multiple functionalization of mesoporous silica nanoparticles: homogeneous implementation of pairs of functionalities communicating through energy or proton transfers. Nanoscale 7:11444–11452
9. Townson JL, Lin YS, Agola JO, Carnes EC, Leong HS, Lewis JD, Haynes CL, Brinker CJ (2013) Re-examining the size/charge paradigm: differing in vivo characteristics of size and charge-matched mesoporous silica nanoparticles. J Am Chem Soc 135:16030
10. Lammers T, Kiessling F, Ashford M, Hennink W, Crommelin D, Storm G (2016) Cancer nanomedicine: is targeting our target? Nat Rev Mater 1:16069

11. Croissant JG, Fatieiev Y, Khashab NM (2017) Degradability and clearance of silicon, organosilica, silsesquioxane, silica mixed oxide, and mesoporous silica nanoparticles. Adv Mater 29:1604634

12. Feng Y, Panwar N, Tng DJH, Tjin SC, Wang K, Yong K-T (2016) The application of mesoporous silica nanoparticle family in cancer theranostics. Coord Chem Rev 319:86–109

13. Butler KS, Durfee PN, Theron C, Ashley CE, Carnes EC, Brinker CJ (2016) Protocells: modular mesoporous silica nanoparticle-supported lipid bilayers for drug delivery. Small 12:2173–2185

14. Lu Y, Fan H, Stump A, Ward TL, Rieker T, Brinker CJ (1999) Aerosol-assisted self-assembly of mesostructured spherical nanoparticles. Nature 398:223–226

15. Croissant JG, Qi C, Maynadier M, Cattoën X, Wong Chi Man M, Raehm L, Mongin O, Blanchard-Desce M, Garcia M, Gary-Bobo M, Durand J-O (2016) Multifunctional gold-mesoporous silica nanocomposites for enhanced two-photon imaging and therapy of cancer cells. Front Mol Biosci 3:1

16. Wang F, Chen X, Zhao Z, Tang S, Huang X, Lin C, Cai C, Zheng N (2011) Synthesis of magnetic, fluorescent and mesoporous core-shell-structured nanoparticles for imaging, targeting and photodynamic therapy. J Mater Chem 21:11244–11252

17. Fatieiev Y, Croissant J, Alamoudi K, Khashab N (2017) Cellular internalization and biocompatibility of periodic mesoporous organosilica nanoparticles with tunable morphologies: from nanospheres to nanowires. ChemPlusChem 82:631–637

18. Yang X, He D, He X, Wang K, Tang J, Zou Z, He X, Xiong J, Li L, Shangguan J (2016) Synthesis of hollow mesoporous silica nanorods with controllable aspect ratios for intracellular triggered drug release in cancer cells. ACS Appl Mater Interfaces 8:20558–20569

19. Croissant JG, Cattoën X, Wong Chi Man M, Durand JO, Khashab NM (2015) Syntheses and applications of periodic mesoporous organosilica nanoparticles. Nanoscale 7:20318–20334

20. Bürglová K, Noureddine A, Hodačová J, Toquer G, Cattoën X, Wong Chi Man M (2014) A general method for preparing bridged organosilanes with pendant functional groups and functional mesoporous organosilicas. Chem Eur J 20:10371–10382

21. Noureddine A, Trens P, Toquer G, Cattoën X, Wong Chi Man M (2014) Tailoring the hydrophilic/lipophilic balance of clickable mesoporous organosilicas by the copper-catalyzed azide–alkyne cycloaddition click-functionalization. Langmuir 30:12297–12305

22. Sun B, Pokhrel S, Dunphy DR, Zhang H, Ji Z, Wang X, Wang M, Liao YP, Chang CH, Dong J, Li R, Mädler L, Brinker CJ, Nel AE, Xia T (2015) Reduction of acute inflammatory effects of fumed silica nanoparticles in the lung by adjusting silanol display through calcination and metal doping. ACS Nano 9:9357–9372

23. Zhang H, Dunphy DR, Jiang X, Meng H, Sun B, Tarn D, Xue M, Wang X, Lin S, Ji Z, Li R, Garcia FL, Yang J, Kirk ML, Xia T, Zink JI, Nel A, Brinker CJ (2012) Processing pathway dependence of amorphous silica nanoparticle toxicity: colloidal vs pyrolytic. J Am Chem Soc 134:15790–15804

24. Noureddine A, Brinker CJ (2018) Pendant/bridged/mesoporous silsesquioxane nanoparticles: versatile and biocompatible platforms for smart delivery of therapeutics. Chem Eng J 340:125–147

25. Ruehle B, Saint-Cricq P, Zink JI (2016) Externally controlled nanomachines on mesoporous silica nanoparticles for biomedical applications. ChemPhysChem 17:1769–1779

26. Ferris DP, Zhao YL, Khashab NM, Khatib HA, Stoddart JF, Zink JI (2009) Light-operated mechanized nanoparticles. J Am Chem Soc 131:1686–1688

27. Noureddine A, Gary-Bobo M, Lichon L, Garcia M, Zink JI, Wong Chi Man M, Cattoën X (2016) Bis-clickable mesoporous silica nanoparticles: straightforward preparation of light-actuated nanomachines for controlled drug delivery with active targeting. Chem Eur J 22:9624–9630

28. Croissant JG, Zink JI, Raehm L, Durand JO (2018) Two-photon-excited silica and organosilica nanoparticles for spatiotemporal cancer treatment. Adv Healthc Mater 7:1701248

29. Omar H, Croissant JG, Alamoudi K, Alsaiari S, Alradwan I, Majrashi MA, Anjum DH, Martins P, Laamarti R, Eppinger J, Moosa B, Almalik A, Khashab NM (2017) Biodegradable magnetic silica@iron oxide nanovectors with ultra-large mesopores for high protein loading, magnetothermal release, and delivery. J Control Rel 259:187–194

30. Baeza A, Guisasola E, Ruiz-Hernandez E, Vallet-Regí M (2012) Magnetically triggered multidrug release by hybrid mesoporous silica nanoparticles. Chem Mater 24:517–524

31. Thomas CR, Ferris DP, Lee JH, Choi E, Cho MH, Kim ES, Stoddart JF, Shin JS, Cheon J, Zink JI (2010) Noninvasive remote-controlled release of drug molecules in vitro using magnetic actuation of mechanized nanoparticles. J Am Chem Soc 132:10623–10625

32. Lee BY, Li Z, Clemens DL, Dillon BJ, Hwang AA, Zink JI, Horwitz MA (2016) Redox-triggered release of moxifloxacin from mesoporous silica nanoparticles functionalized with disulfide snap-tops enhances efficacy against pneumonic tularemia in mice. Small 12:3690–3702

33. Croissant JG, Fatieiev Y, Julfakyan K, Lu J, Emwas AH, Anjum DH, Omar H, Tamanoi F, Zink JI, Khashab NM (2016) Biodegradable oxamide-phenylene-based mesoporous organosilica nanoparticles with unprecedented drug payloads for delivery in cells. Chem Eur J 22:14806–14811

34. Llopis-Lorente A, Lozano-Torres B, Bernardos A, Martínez-Máñez R, Sancenón F (2017) Mesoporous silica materials for controlled delivery based on enzymes. J Mater Chem B 5:3069–3083

35. Wan X, Zhang G, Liu S (2011) pH-disintegrable polyelectrolyte multilayer-coated mesoporous silica nanoparticles exhibiting triggered co-release of cisplatin and model drug molecules. Macromol Rapid Commun 32:1082–1089

36. Meng H, Xue M, Xia T, Zhao YL, Tamanoi F, Stoddart JF, Zink JI, Nel AE (2010) Autonomous in vitro anticancer drug release from mesoporous silica nanoparticles by pH-sensitive nanovalves. J Am Chem Soc 132:12690–12697

37. Croissant JG, Zhang D, Alsaiari S, Lu J, Deng L, Tamanoi F, AlMalik AM, Zink JI, Khashab NM (2016) Protein-gold clusters-capped mesoporous silica nanoparticles for high drug loading, autonomous gemcitabine/doxorubicin co-delivery, and in-vivo tumor imaging. J Control Rel 229:183–191

38. Croissant JG, Fatieiev Y, Omar H, Anjum DH, Gurinov A, Lu J, Tamanoi F, Zink JI, Khashab NM (2016) Periodic mesoporous organosilica nanoparticles with controlled morphologies and high drug/dye loadings for multicargo delivery in cancer cells. Chem Eur J 22:9607–9615

39. Liu J, Stace-Naughton A, Jiang X, Brinker CJ (2009) Porous nanoparticle supported lipid bilayers (protocells) as delivery vehicles. J Am Chem Soc 131:1354

40. Ashley CE, Carnes EC, Phillips GK, Padilla D, Durfee PN, Brown PA, Hanna TN, Liu J, Phillips B, Carter MB, Carroll NJ, Jiang X, Dunphy DR, Chackerian CL, Wharton W, Peabody DS, Brinker CJ (2011) The targeted delivery of multicomponent cargos to cancer cells by nanoporous particle-supported lipid bilayers. Nat Mater 10:389–397

41. Villegas MR, Baeza A, Noureddine A, Durfee PN, Butler KS, Agola JO, Brinker CJ, Vallet-Regí M (2017) Multifunctional protocells for enhanced penetration in 3D extracellular tumoral matrices. Chem Mater 30:112–120

42. Liu J, Jiang X, Ashley C, Brinker CJ (2009) Electrostatically mediated liposome fusion and lipid exchange with a nanoparticle-supported bilayer for control of surface charge, drug containment, and delivery. J Am Chem Soc 131:7567

43. Judeinstein P, Sanchez C (1996) Hybrid organic–inorganic materials: a land of multidisciplinarity. J Mater Chem 6:511–525

44. Liu X, Situ A, Kang Y, Villabroza KR, Liao Y, Chang CH, Donahue T, Nel AE, Meng H (2016) Irinotecan delivery by lipid-coated mesoporous silica nanoparticles shows improved efficacy and safety over liposomes for pancreatic cancer. ACS Nano 10:2702–2715

45. Epler K, Padilla D, Phillips G, Crowder P, Castillo R, Wilkinson D, Wilkinson B, Burgard C, Kalinich R, Townson J, Chackerian B (2012) Delivery of ricin toxin a-chain by peptide-targeted mesoporous silica nanoparticle-supported lipid bilayers. Adv Healthc Mater 1:348–353

46. Meng H, Wang M, Liu H, Liu X, Situ A, Wu B, Ji Z, Chang CH, Nel AE (2015) Use of a lipid-coated mesoporous silica nano-particle platform for synergistic gemcitabine and paclitaxel delivery to human pancreatic cancer in mice. ACS Nano 9:3540–3557

47. Slaughter BV, Lino CA, McBride AA, Fleig PF, Conroy MA, Melo CF, Wilkinson BS, Garcia GU, Wu TU, Adolphi NU, Reed S (2016) Mesoporous silica nanoparticle-supported lipid bilayers for targeted antibiotic therapeutics. Sandia National Laboratories (SNL-NM), Albuquerque, NM

48. Dengler EC, Liu J, Kerwin A, Torres S, Olcott CM, Bowman BN, Armijo L, Gentry K, Wilkerson J, Wallace J, Jiang X, Carnes EC, Brinker CJ, Milligan ED (2013) Mesoporous silica-supported lipid bilayers (protocells) for DNA cargo delivery to the spinal cord. J Control Rel 168:209–224

49. Zhao D, Feng J, Huo Q, Melosh N, Frederickson GH, Chmelka BF, Stucky GD (1998) Triblock copolymer syntheses of meso-porous silica with periodic 50 to 300 angstrom pores. Science 279:548–552

50. Knezevic NZ, Durand J-O (2015) Large pore mesoporous silica nanomaterials for application in delivery of biomolecules. Nanoscale 7:2199–2209

51. Yang J, Zhang F, Li W, Gu D, Shen D, Fan J, Zhang WX, Zhao D (2014) Large pore mesostructured cellular silica foam coated magnetic oxide composites with multilamellar vesicle shells for adsorption. Chem Commun 50:713–715

52. Shin H-S, Hwang Y-K, Huh S (2014) Facile preparation of ultra-large pore mesoporous silica nanoparticles and their application to the encapsulation of large guest molecules. ACS Appl Mater Interfaces 6:1740–1746

53. Gao Z, Zharov I (2014) Large pore mesoporous silica nano-particles by templating with a nonsurfactant molecule, tannic acid. Chem Mater 26:2030–2037

54. Mandal M, Manchanda AS, Zhuang J, Kruk M (2012) Face-centered-cubic large-pore periodic mesoporous organosilicas with unsaturated and aromatic bridging groups. Langmuir 28:8737–8745

55. Rosenholm JM, Zhang J, Sun W, Gu H (2011) Large-pore mesoporous silica-coated magnetite core-shell nanocomposites and their relevance for biomedical applications. Microporous Mesoporous Mater 145:14–20

56. Gao F, Botella P, Corma A, Blesa J, Dong L (2009) Mono-dispersed mesoporous silica nanoparticles with very large pores for enhanced adsorption and release of DNA. J Phys Chem B 113:1796–1804

57. Zhang J, Li X, Rosenholm JM, Gu H-c (2011) Synthesis and characterization of pore size-tunable magnetic mesoporous silica nanoparticles. J Colloid Interface Sci 361:16–24

58. Wu M, Meng Q, Chen Y, Zhang L, Li M, Cai X, Li Y, Yu P, Zhang L, Shi J (2016) Large pore-sized hollow mesoporous organosilica for redox-responsive gene delivery and synergistic cancer chemotherapy. Adv Mater 28:1963–1969

59. Chen Y, Chu C, Zhou Y, Ru Y, Chen H, Chen F, He Q, Zhang Y, Zhang L, Shi J (2011) Reversible pore-structure evolution in hollow silica nanocapsules: large pores for siRNA delivery and nanoparticle collecting. Small 7:2935–2944

60. Wu M, Meng Q, Chen Y, Du Y, Zhang L, Li Y, Zhang L, Shi J (2015) Large-pore ultrasmall mesoporous organosilica nano-particles: micelle/precursor co-templating assembly and nuclear-targeted gene delivery. Adv Mater 27:215–222

61. Song HM, Zink JI, Khashab NM (2015) Engineering the internal structure of magnetic silica nanoparticles by thermal control. Part Part Syst Charact 32:307–312

62. Shen D, Yang J, Li X, Zhou L, Zhang R, Li W, Chen L, Wang R, Zhang F, Zhao D (2014) Biphase stratification approach to three-dimensional dendritic biodegradable mesoporous silica nano-spheres. Nano Lett 14:923–932